View Article Online
DOI: 10.1039/D0NJ02914A

HYDROGEN BONDING INTERACTIONS IN FLUORINATED 1,2,3-TRIAZOLE DERIVATIVES

E. Espitia Cogollo,[a] O.E. Piro,[b] G.A. Echeverría,[b] M.E Tuttolomondo,[c] H. Pérez,[d] J.L. Jios[e,f*] and S.E. Ulic,[a,g*]

[a.] *CEQUINOR (CONICET-UNLP), Facultad de Ciencias Exactas, Universidad Nacional de La Plata, Bv. 120 N° 1465, 1900 La Plata, Argentina*

[b.] *Departamento de Física, Facultad de Ciencias Exactas, Universidad Nacional de La Plata e IFLP (CONICET, CCT-La Plata), C. C. 67, 1900 La Plata, Argentina*

[c.] *[1]INQUINOA-CONICET, Instituto de Química Física, Facultad de Bioquímica, Química y Farmacia, Universidad Nacional de Tucumán, Argentina.*

[d.] *Departamento de Química Inorgánica, Facultad de Química, Universidad de La Habana, La Habana 10400, Cuba.*

[e.] *Laboratorio UPL (UNLP-CIC), Campus Tecnológico Gonnet (CIC-BA), Cno. Centenario e/505 y 508, (1897) Gonnet, Argentina.*

[f.] *Departamento de Química, Facultad de Ciencias Exactas, Universidad Nacional de La Plata, 47 esq. 115, (1900) La Plata, Argentina.*

[g.] *Departamento de Ciencias Básicas, Universidad Nacional de Luján, Rutas 5 y 7, 6700 Luján, Buenos Aires, Argentina*

**To whom correspondence should be addressed: jljios@quimica.unlp.edu.ar; sonia@quimica.unlp.edu.ar*

Abstract

The study of intra- and intermolecular interactions in solid state of four related fluorine-containing 1,2,3-triazole derivatives (**1**: R= -H, **2**: R= -NO_2, **3**: R= -CH_3, **4**: R= -Cl) was carried out using quantum chemical calculations, vibrational (IR and Raman) and solid phase UV-Vis spectroscopy, and single-crystal X-ray diffraction methods. The enol-keto / keto-enol tautomerism on the *o*-hydroxyacetophenone moiety was analyzed in terms of the synergy between O-H···O intramolecular hydrogen bond strengthening and the enhancement of π delocalization within the pseudo ring. The preference of the enol-keto form was attributed to the aromatic stabilization energy. The proton in the triazole ring was located on the intermediate nitrogen atom, with no evidence of prototropie in the studied series. Compounds **1** and **4** have similar structural motifs with N-H···O hydrogen bonds connecting amino and carbonyl groups of neighboring molecules in a chain along *a*-axis. For **2**, it was

View Article Online
DOI: 10.1039/D0NJ02914A

found that both oxygen atoms of the nitro substituent participate as acceptors, connecting adjacent molecules by hydrogen bonds through the N-H and O-H groups. In compound **3**, the crystallization water molecule dominates the hydrogen bonding interactions, which associates three molecules of **3**, giving rise to a three-dimensional H-bonding network. These intra and intermolecular interactions, which affect the absorption bands location of the involved groups, were also detected in the vibrational spectra of the studied triazole.

Keywords: X-ray crystal structure, molecular interactions, NBO intermolecular energies, Hirshfeld surface analysis, Pixel energies, vibrational spectroscopy

View Article Online
DOI: 10.1039/D0NJ02914A

1.Introduction

Five-membered ring heterocycles containing three consecutive nitrogen atoms are known as 1,2,3-triazoles or vicinal triazoles.[1] Its chemistry has been revalued since the appearance of click-chemistry, which significantly improved the reaction conditions for the synthesis of these heterocycles.[2,3]

1,2,3-Triazoles are recognized by its medicinal significance due to their wide range of bioactivity. As biologically active molecules, among the most relevant, they demonstrated anti-cancer, anti-inflammatory, antitubercular, antileishmanial, antitrypanosomal, antimicrobial, antiviral, and antibacterial activity.[4–6] Some structural properties of triazoles such as high dipole moment value, the presence of acceptor nitrogen atoms and donor N-H hydrogen groups, and a rich electron aromatic (π-excessive) ring allow them to form dipole-dipole, hydrogen bonding and π stacking interactions. Such properties are of great importance in the field of medicinal chemistry, because they improve the binding with the biological target. Structural studies of 1,2,3-triazoles are necessary to fully understand their properties. They are widely used as a bioisoster for the design of drug analogues due to an additional advantage: their marked stability under hydrolytic, oxidative, and reducing conditions. This ring has been used primarily as an amide and ester isostere and allows, for example, to reduce the compounds' in vivo susceptibility to enzymatic degradation.[7]

Besides, the inclusion of fluorine atoms in its structure, enhance their molecular properties and biological activities. Its high electron affinity, lipophilicity and bioavailability extends the half-life of the drugs.[8–10] Also, the application of fluoride in the design of drugs is related to its ability to increase metabolic stability or influence the metabolism of the molecule.[11] Within the fluorinated drugs, perfluoromethyl substituted compounds have demonstrated a notable high activity against the malaria parasite.[10] Vicinal triazoles without substitution on the nitrogen atom can be obtained by reacting sodium azide with α and γ pyrones.[12,13] This synthetic route is simple and allows the construction of new heterocyclic structures substituted with trifluoromethyl groups possessing interesting properties. For this purpose, chromone is used as a source of γ pyrone, with the advantage that trifluorochromones are obtained in a one-step simple way.[14,15]

In this work, the synthesis and study of four 4-(2'-hydroxybenzoyl)-5-trifluoromethyl-2H-1,2,3-triazoles is presented (scheme 1). On the heterocycle, the hydrogen location in one of the three nitrogen atoms (prototropie) depends on the molecule structure, its aggregation state and the solvent used when they are analyzed in solution.[1,16] The triazoles presented in this work were studied in solid state, mainly using X-ray diffraction methods.

View Article Online
DOI: 10.1039/D0NJ02914A

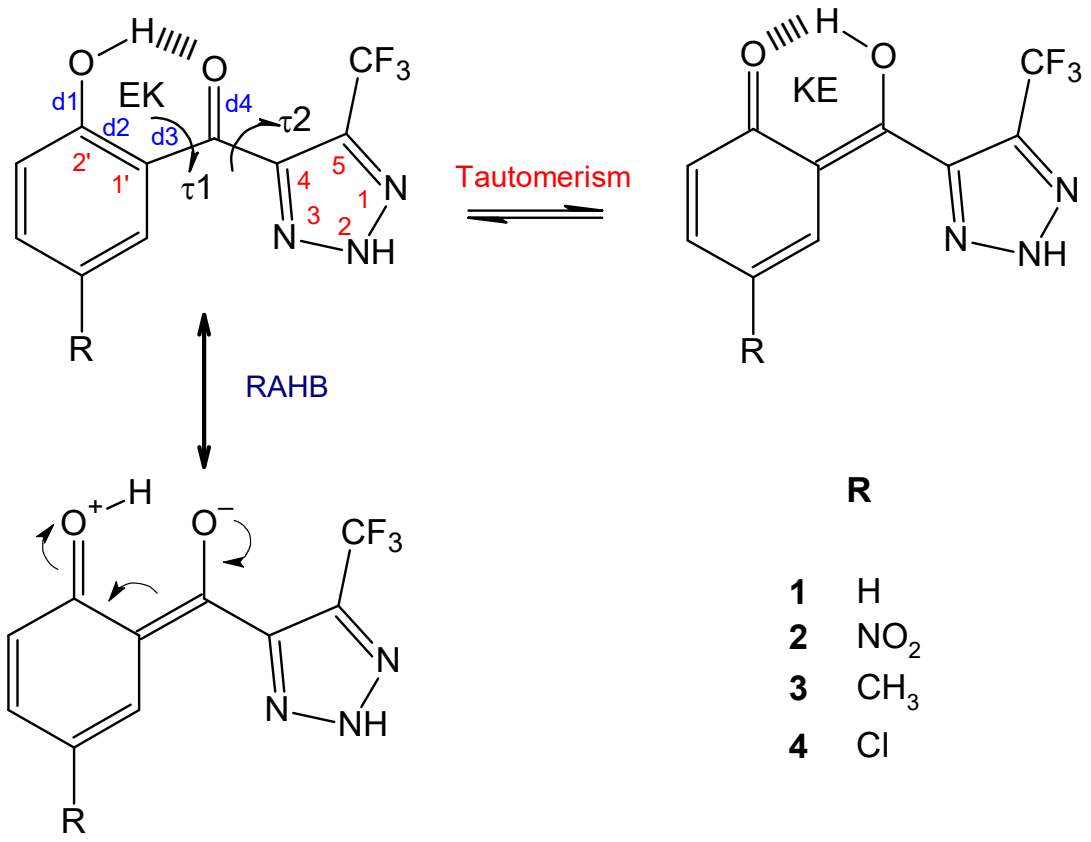

R

1	H
2	NO_2
3	CH_3
4	Cl

Scheme 1: Hydrogen bonding in the studied triazoles involving the enol-keto (EK, left) and keto-enol (KE, right) forms in equilibrium (tautomerism) and the uncharged (upper) and ionized (lower) mesomeric structures (RAHB concept). The d1-d4 and τ1-τ2 are the selected π-conjugated bonds and torsion angles connecting aromatic planes with the carbonyl central group, respectively.

The structures are dominated by intra and intermolecular O-H···O hydrogen bond interactions, whose strength and geometry are sensitive to the substituents. The study was complemented with vibrational spectroscopy (IR and Raman) and theoretical calculations. A complete characterization and a tentative assignment of the vibrational spectra were performed using reported data of related compounds and the calculated frequencies after geometry optimization.[17,18]

In this series of triazoles, the phenyl-substituted (2-hydroxyphenyl)carbonyl fragment consists of a β-diketone enol group (β-enol keto group) asymmetrically fused to a phenyl ring. It is well known the occurrence of extreme HO–C=C–C=O (enol-keto, EK) and O=C–C=C–OH (keto-enol, KE) forms in the keto-enol tautomerism of enolones.[19] An important feature of β-diketones molecular crystals is the packing of the enol tautomers, stabilized by strong intramolecular O-H···O resonance-assisted hydrogen bond (RAHB).[20–24] Following

View Article Online
DOI: 10.1039/D0NJ02914A

Gilli's foundational work,[20] its RAHB concept has also been successfully applied for other π-conjugated compounds as 2-hydroxybenzoketones.[25]

In the RAHB system, the proton acceptor and proton donor groups are connected through a chain of delocalized conjugated double bonds d1-d4, stabilizing the molecular system (resonance concept). Because of the electron density transfer in the resonance structures, the hydrogen acceptor turn into the hydrogen donor and vice versa (see Scheme 1).

However, though the concept of RAHB has been widely accepted, at present there are controversies in the literature about its nature.[26,27] In special with the role of the electron delocalization in the system.[28] Thus, theoretical calculations have suggested for unsaturated compounds the formation of stronger intramolecular hydrogen bonds than in their saturated analogues, not only through a resonance mechanism but also as a result of steric strain or constraints associated to the σ-skeleton.[29] Recent studies showed that substituents can weaken intramolecular hydrogen bonds, affecting RAHB and favoring intermolecular interactions.[30] Both inter- and intramolecular noncovalent interactions are crucial in determining the molecular organization of the compounds in solution and solid state. This fact, considering also the relevant role of intramolecular H-bond in biological and chemical processes,[31] prompted to analyze the resonance effect on the intramolecular O-H···O interactions strength for the four structures reported in this work.

Lattice and intermolecular interaction energies associated to different molecular pairs were calculated in order to determine the energy components contributing to crystal stabilization.[32] Hirshfeld surfaces analysis[33] has been used to explore the packing modes and the visualization of intermolecular interactions. Quantitative pictures of intermolecular contacts, including the relative percentage for each interaction type and their enrichment ratios, were obtained from fingerprint plots and their decompositions.[34]

2. Experimental

2.1. Synthesis

The title compounds were synthesized from the respective 2-trifluoromethylchromones (TFMC)[12,13] and 6-nitro-2-trifluoromethylchromone.[35] TFMC were prepared following the one-pot procedure reported by Henao Castañeda.[14,15]

View Article Online
DOI: 10.1039/D0NJ02914A

2.2. Instrumentation

2.2.1. X-ray diffraction data

The measurements were performed on a Rigaku-Oxford Gemini diffractometer equipped with an Eos CCD detector and a graphite-monochromated MoKα (λ= 0.71073 Å) radiation. X-ray diffraction intensities were collected (ω scans with ϑ and κ-offsets), integrated and scaled with CrysAlisPro[36] suite of programs. The unit cell parameters were obtained by least-squares refinement (based on the angular settings for all collected reflections with intensities larger than seven times the standard deviation of measurement errors) using CrysAlisPro. Data were empirically corrected for absorption, employing the multi-scan method implemented in CrysAlisPro.

The structures were solved by intrinsic phasing with SHELXT of the SHELX suit of programs.[37] and the molecular model refined by full-matrix least-squares procedure with SHELXL of the same package. The hydrogen atoms of compounds **1**, **2** and **4** were located from difference Fourier maps and refined at their found positions with isotropic displacement parameters. All but the hydroxyl and water hydrogen atoms of compound **3** were positioned on stereo-chemical basis and refined with the riding model. The H-atoms of $–CH_3$ group were treated as a rigid group allowed to rotate during the refinement around the $C–CH_3$ bond as to maximize the sum of the residual electron density at the calculated positions. The hydroxyl and water H-atoms were located in a difference Fourier map and refined at their found positions with isotropic displacement parameters. Crystal data, data collection procedure and refinement results are summarized in Table S1 (ESI†).

Crystallographic structural data for all four compounds have been deposited at the Cambridge Crystallographic Data Centre (CCDC). Enquiries for data can be direct to: Cambridge Crystallographic Data Centre, 12 Union Road, Cambridge, UK, CB2 1EZ or (e-mail) deposit@ccdc.cam.ac.uk or (fax) +44 (0) 1223 336033. Any request to the Cambridge Crystallographic Data Centre for these materials should quote the full literature citation and the reference number CCDC 1589636 (**1**), CCDC 1589637 (**2**), CCDC 1589638 (**3**) and CCDC 1936976 (**4**). The molecular geometries were calculated using WinGX[38], and PLATON for Windows Taskbar v1.17.[39,40], ORTEP-3[41] and Mercury[42] programs were used for molecular graphics.

2.2.2. Infrared and Raman Spectroscopy

Infrared absorption spectra (KBr pellets) were recorded on a LUMEX InfraLUM FT-02 spectrometer and on a FTIR Instrument Bruker Equinox, with a resolution of 2 cm^{-1} from 4000 to 400 cm^{-1}. The Raman spectra of the solid were performed in the range 3500-100

View Article Online
DOI: 10.1039/D0NJ02914A

cm^{-1} at room temperature on a Thermoscientific DXR Raman microscope, using a diode-pump and a 780 nm solid-state laser, with spectral resolution of 5 cm^{-1}.

2.2.3. Electronic spectra

Diffuse reflectance UV-Vis spectra were recorded on a Shimadzu UV-2600 Spectrophotometer in the spectral region of 200-900 nm, using $BaSO_4$ as reference.

2.3. Computational methods

2.3.1. Lattice and interaction energies

For each crystal structure under consideration, lattice and intermolecular interaction energies for specific molecular pairs were calculated using the CLP (Coulomb–London–Pauli) approach implemented in the PIXEL program package.[43,44] It enables the partitioning of the total energy into their coulombic, polarization, dispersion and repulsion contributions from the knowledge of the electronic charge density of the free molecule. Accurate electron densities around the molecules were calculated at MP2/6-31G** level using Gaussian 03.[45]

2.3.2. Hirshfeld surface calculations

Hirshfeld surfaces (HSs) and their associated two-dimensional fingerprint plots (FPs)[46–48] were plotted using CrystalExplorer3.0.[49] The d_{norm} (normalized contact distance) surface and the breakdown of two-dimensional fingerprint plots were used for decoding and quantifying intermolecular interactions in the crystal lattice. The d_{norm} is a symmetric function of distances to the surface from nuclei inside and outside the HS (di and de, respectively), relative to their respective van der Waals radii (r_{vdW}), which allows identification of the regions of particular importance to intermolecular interactions. The d_{norm} surfaces were mapped over a fixed color scale of -0.078 au (red) – 0.657 au (blue). Other two-colored properties (Curvedness and Shape Index) based on the local curvature of the surface were also analyzed. The former is a measure of “how much shape” (low values related with flat surface areas, and areas of sharp curvature have a high curvedness), and the latter is a measure of “which shape”. The FPs were displayed by using the standard 0.6–2.4 Å (compound **1**), translated 1.0–2.8 Å (compound **2**) and expanded 0.6–2.8 Å (compounds **3** and **4**) ranges, and reciprocal contacts were included.

2.3.3. Quantum chemical calculations

Quantum chemical calculations were performed with the program package Gaussian 03.[45] The relaxed potential energy surface scans, geometry optimizations and vibrational frequency calculations were performed with the Density Functional Theory (DFT)[50] method

View Article Online
DOI: 10.1039/D0NJ02914A

employing the 6-31g(d,p), 6-311g(d,p)[51] and cc-pVDZ[52] basis sets. The vibrational and electronic spectra of all compounds were computed with B3LYP/6-31g(d,p) level of theory, starting from the optimized geometries using the 6-31g(d,p) basis set, since the calculated spectra fit better with the experimental ones.[53]

The calculated vibrational properties correspond to real minima on the potential energy surface, with no imaginary frequencies. Natural Bond Orbital (NBO) analysis,[54] as implemented in the Gaussian 03 package, was performed at B3LYP/cc-pVDZ level for the **1** – **4** monomeric and dimers structures, in order to obtain second-order donor → acceptor interaction energies.

3. Results and discussion

3.1. Molecular structure description

ORTEP drawings of **1** – **4** are shown in Figures 1a-d. In all compounds, the trifluoromethyl group adopts a nearly staggered angular conformation, and average C-F and F-C-F bond distances and angles are: 1.325(3) Å and 106.7(5)º, and average C-C-F bond angle is 112.1(3)º, as reported for similar compounds.[55] Differing only in substitutions on the phenyl ring, the molecules are structurally close to each other. Their conformations are determined by relatively unhindered rotations around the C(phe)-(C=O) and (O=C)-C(trz) σ-bonds [bond lengths: 1.461(2) and 1.488(2) Å for **1**; 1.467(4) and 1.484(3) Å for **2**; 1.458(3) and 1.486(3) Å for **3**; and 1.453(3) and 1.490(4) Å for **4**]. Within the aromatic triazole, the C-C, C9-N1 (C9-N4 for **2**), and C8-N3 (C8-N2 for **2**) distances are between 1.397 Å – 1.408 Å, 1.324 Å – 1.336 Å, and 1.336 Å – 1.340 Å, respectively. The C-N bond lengths are longer than that expected for formally imino C=N bond character. Although the sp^2-hybridized C-C distance is greater than the C-N bonds, the former is shorter than the C7-C8 sp^2 exocyclic bond discussed above (1.484 Å – 1.490 Å). That is consistent with the charge delocalization expected for this aromatic heterocyclic moiety.

In all compounds, the τ_2 torsion angle connecting the carbonyl and the phenyl ring (scheme 1) is close to 0º [ranging from +4.2(4)º in compound **2** to -10.7(4)º in **4**], and hence a nearly planar structure in the (2-hydroxyphenyl)carbonyl fragment is preferred. In this conformation, the C=O and O−H groups form a pseudo-six-membered ring favoring a strong O–H···(O=C) intramolecular hydrogen bond (IMHB), as shown in Figures 1a-d. Both oxygen atoms are connected by a π-conjugated β-diketone enol system, wherein the O–H···O bond is presumably assisted by resonance (RAHB).[20–24]

The relative occurrence of both tautomeric forms in enolones can be analyzed in terms of synergism between O-H···O hydrogen-bond strengthening (as determined by the O···O

View Article Online
DOI: 10.1039/D0NJ02914A

distance) and π-delocalization enhancing as considered by: a) asymmetric stretching coordinate $Q = d_1-d_4+d_3-d_2$, where d_i are actual bond distances (see Scheme 1); b) π-delocalization index $\lambda = 1-[(n_1-1)+(2-n_2)+(n_3-1)+(2-n_4)]/4$,[56] where n_i are the Pauling's bond numbers[57] calculated as $d(1) - d(n) = c \log 10n$, with values for pure single (n = 1) and double (n = 2) bond distances of (1.467–1.349) Å and (1.367–1.217) Å for Csp^2—Csp^2 and Csp^2—O bonds, respectively, and c) percent delocalization Del%=100(1-|2λ-1|) induced by RAHB in the resonant fragment. The λ index is associated to the percent contributions of EK and KE forms. Q (λ) varies from $Q = Q_o$= 0.320 Å (λ = 1.0) to $Q = Q_o$= -0.320 Å (λ = 0) for the totally π-localized EK and KE tautomers, respectively, being Q = 0 (λ= 0.5) and Del% = 100 for complete delocalization of the π-conjugated fragment (1:1 mixture of EK and KE).

The IMHB geometrical parameters of all molecules are given in Table 1.

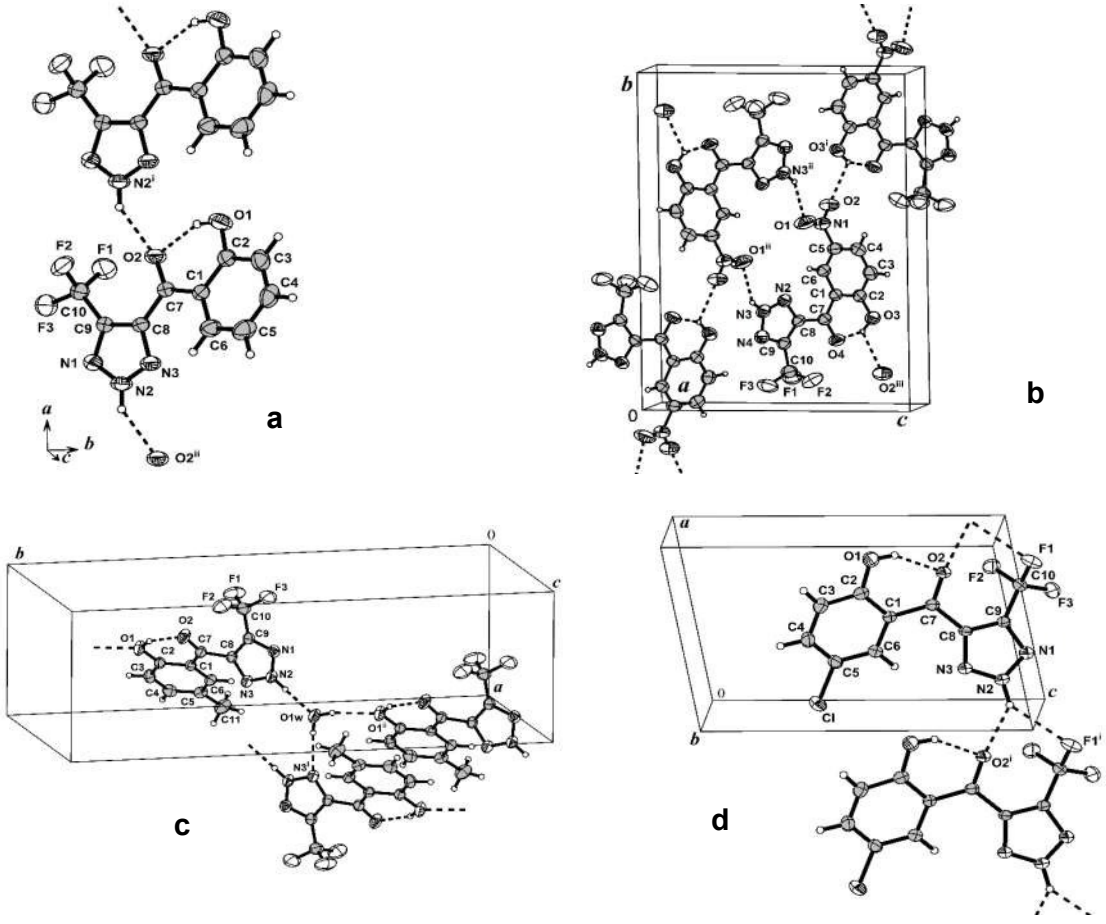

Figure 1. **a)** View of the crystal packing for **1** showing the labeling of the non-H atoms and their displacement ellipsoids at the 50% probability level. H-bonds are indicated by dashed lines. Space group symmetry operations: (i) 1+x, y, z; (ii) -1+x, y, z. **b) 2** (50% probability level; (i) 3/2-x, ½'y, 3/2-z; (ii) –x, 1-y, 1-z; (iii) 3/2-x, -1/2+y, 3/2-z) **c) 3** (30% probability level; (i) 2-x, 1-y, 1-z; (ii) 1/2+x, -1/2+y, z) and **d) 4** (30% probability level; (i) x-1, y, z).

View Article Online
DOI: 10.1039/D0NJ02914A

Table 1. Intramolecular O–H···O hydrogen bond geometry (Å,°), d_1-d_4[a] bond distances (Å), Pauling's bond numbers *n*[b], and π-delocalization parameters (*Q*, λ and Del%) for **1** – **4**.

Comp.	d_{O-H}	$d_{O\cdots O}$	$d_{H\cdots O}$	$\angle_{O-H\cdots O}$	d_1	d_2	d_3	d_4	*Q*	λ	Del%
1	0.899	2.584(2)	1.78(3)	147(3)	1.343	1.413	1.461	1.235	0.156	0.763	47.4
					1.12	*1.37*	*1.04*	*1.84*			
2	0.986	2.543(3)	1.64(4)	150(4)	1.337	1.421	1.467	1.231	0.152	0.760	48.0
					1.15	*1.31*	*1.00*	*1.88*			
3	0.873	2.537(2)	1.74(3)	150(3)	1.356	1.405	1.458	1.233	0.176	0.800	40.0
					1.05	*1.44*	*1.05*	*1.86*			
4	0.817	2.614(3)	1.88(4)	149(3)	1.338	1.410	1.453	1.239	0.142	0.745	51.0
					1.14	*1.40*	*1.09*	*1.81*			

[a] See Scheme 1 for d_1-d_4 labels. [b] Pauling's bond numbers n ($1 \le n \le 2$) are in italic.

Taking into account the d(O···O) distance, as indicator of length and strength,[22] the O-H···O IMHB can be classified as strong for all four compounds [($2.50 \le d(O\cdots O) \le 2.65$ Å)], being the O···O distances systematically shorter than those for compounds with non-resonant hydrogen bonds [($2.59 \le d(O\cdots O) \le 2.64$ Å)].[23] The O-H-O angles are in the range 149 ± 5^o (Table 1), characteristic of intramolecular bonds closing six membered rings.[22] Spectroscopic results provide also evidences of the abnormal shortening of O-H···O IMHB for **1** – **4**. Thus, the ν(OH) frequencies (3331-3180 cm^{-1}, see Section **3.6**)) are lower than 3640 cm^{-1}, in absence of hydrogen bond.[21] Moreover, the downfield shifts (11.59-12.35 ppm) of the hydroxyl proton ^{1}H NMR signals (results to be published), related to the 8.6-10.1 ppm range where π-resonance does not occurs,[23] can be ascribed to the d(O···O) shortening. Both descriptors are indicative of the hydrogen bond strength.

In the aim to verify the role of π-resonance in the strengthening of O-H···O IMHB for **1** – **4** in solid state, the d_1-d_4 bond distances, antisymmetric stretching coordinate (*Q*), π-delocalization index (λ), and percent delocalization (Del%) in the 2-hydroxybenzoketone resonant fragment were computed (Table 1). The high positive values of *Q* (0.142-0.176) indicating no much equalization of C-C, C=C, C=O and C-O bonds, and the high values of λ (0.745-0.800) near to unity, show a dominant contribution of the enol-keto form (EK). Considering the structures outlined in scheme 1, the keto-enol form (KE) involves the breakdown of the aromatic system and the loss of its stabilization energy, therefore, it is expected that the equilibrium will be strongly shifted to the EK form. Similar behavior was

View Article Online
DOI: 10.1039/D0NJ02914A

reported for a group of eight 2-hydroxybenzoketones, showing O-H···OH-bond assisted by resonance.[23]

Meanwhile, in compound **3** the methyl group releases electrons activating the phenyl ring and hence hindering the resonance as reflected by lower Del% of 40.0%. However, unlike the eight above-mentioned 2-hydroxybenzoketones,[23] the expected linear correlation predicted by the RAHB model was not found between the shortening of O···O distance and the increasing of π-delocalization measured through the descriptors *Q*, λ and Del% for the O-C-C-C-O hydrogen-bonded ring (see Table 1). Surprisingly, for example, the shortest O···O distance of 2.537(2) Å in **3** appears correlated with the lowest Del% (40%) in the series, contrary to the RAHB mechanism. According to these results, it can be concluded that the enhanced strength of the IMHB in compounds **1** – **4** is not a primary consequence of a π-resonance effect, but probably a result of the *σ*-skeleton framework imposing constraints to keep oxygen atoms near to each other, as suggested in recent publications.[27]

3.2. Structural motifs of crystal packing

In Figures 1a-d are shown the ORTEP drawings of the crystal packing for **1** – **4**. Unlike the small variations of τ_2 torsion angle discussed above, τ_1 involving the carbonyl plane and the heterocyclic ring (O2C7-C8C9) seems to be much influenced by intermolecular forces, as suggested by angular values in the wide range from -5.2(2)º to -29.9(3)º. The largest one occurs in hydrate **3**, under the influence of a strong interaction between the donor NH and the acceptor water oxygen atom through a hydrogen bond. In fact, the crystals of **1** – **4** are mostly stabilized by intermolecular hydrogen bonds involving the triazole ring. The main structural motifs corresponding to stronger O–H···O, N–H···O and O–H···N hydrogen bonds are described as follow:

*Compound **1***: Neighbouring molecules related through a unit cell translation along the *a*-axis are N2H2N···O2' bonded to each other [d(NH···O) = 2.11(2) Å, ∠(N–H···O) = 142(2)º], giving rise to a chain structure that extends in the lattice along that crystal axis (see Figure 1a). These chains, resembling ribbons, pack along the *b*-axis through weak intermolecular contacts building corrugated (001) layers. Besides, these layers are connected mainly through offset π-π interactions, developing the 3D crystal structure (see section 3.4 Hirshfeld surfaces analysis for further details).[58]

*Compound **2***: The O1 and O2 atoms of the -NO_2 substituent, with high charge density, concentrate the main intermolecular interactions. Neighbouring molecules, symmetrically related through the crystallographic two-fold screw-axis, connect the hydroxyl proton with

View Article Online
DOI: 10.1039/D0NJ02914A

one oxygen (O2) atom of the nitro group, by a bent O3H3O···O2N1 bond, [d(OH···O) = 2.38(4) Å, ∠(O–H···O) = 112(3)º] hence generating a chain along the unique *b*-axis. The other oxygen atom (O1) participates in adjacent chains, and with additional O···H contacts with the amino N-H group, through N3H3N···O1N1 interactions [d(NH···O) = 2.25(4) Å, ∠(N–H···O) = 145(4)º]. These hydrogen bonds link the molecules into center-symmetric dimers, originating $R_2^2\,(20)$ graph-set motifs producing a layered structure parallel to the crystal (1,0,-3) plane (see Figure 1b), in which two trifluoromethyl groups of adjacent molecules are facing each other (the distance between centroids is 3.580 Å). Therefore, it seems that in **2** the competition between the nitro group and the triazole ring results in an intermolecular hydrogen bonds network different from **1**. Similar to **1**, layers pack through offset π-π interactions building the 3D crystal structure (see section 3.4 for further details).[58]

*Compound **3***: The crystallization water molecule bridges three neighboring molecules: a) as acceptor in a N2H2N···Ow bonds with one molecule [d(N2···Ow) = 2.702(2) Å, ∠(N2-H2N···Ow) = 175º], b) as donor in further OwH···N3' [d(OwH···N3') = 2.15(4) Å, ∠(OwH···N3') = 176(3)º] and OwH···O1" [d(OwH···O1") = 2.08(4) Å, ∠(OwH···O1") = 166(3)º] bonds with other two molecules, giving rise to a three-dimensional H-bonding network (see Fig. 1c). Two water molecules, which interact as donor and acceptor, link the N2-H and N3 atoms of two faced neighboring triazole residues of center-symmetric dimers, originating $R_4^4\,(10)$ graph-set motifs (not shown in Figure 1). Besides, the H-bonding networks are assisted by offset π···π contacts between neighboring molecules, further stabilizing the 3D crystal structure.[58]

*Compound **4***: Neighboring molecules symmetrically related to each other, through a unit cell translation along the *a*-axis, are N2H2N···O2' bonded [d(NH···O') = 2.06(3) Å, ∠(N2-H2N…O2') = 137(2)º] giving rise to a chain structure (similar to that found in **1**) that extends in the lattice (see Figure 1d) like a ribbon. As result, both structures have similar value of the *a*-parameter of the unit cell (see Table S1, ESI†). Furthermore, it seems that along the molecular chain, the geometric requirement of the N2H2N···O2' hydrogen bond places the adjacent molecules very close to each other leaving no room for the chlorine atom in the main molecular plane and forcing chlorophenyl to deviate from it. Therefore, the angle between the phenyl and triazole planes in **4** (36.9°) is greater than in **1** (14.9°)

Along the *c*-axis, ribbons are arranged through weak intermolecular interactions building (0,1,0) layers, which are packed through offset π···π contacts, developing the 3D crystal structure (see section 3.4).

View Article Online
DOI: 10.1039/D0NJ02914A

In summary, the influence of the substituent on the conformation adopted for the molecule in the crystal lattice is strongly dependent of its acceptor capacity. The -H and -Cl substituent (compounds **1** and **4**) have a similar behavior on the supramolecular assembly, which is dominated by the intermolecular N-H···O=C interactions. The carbonyl oxygen atom is a better acceptor and short interatomic N···O values of 2.06 Å (**4**) and 2.11 Å (**1**) are obtained. That explains the weakening of the RAHB interaction as observed in Table 1 with the lengthening of the $d_{O\cdots O}$ distance. In **3**, the effect of the -CH3 substituent is masked by the water molecule, that acts as strong donor-acceptor group. Like the nitro group in **2**, the intermolecular interactions are controlled by these groups. Now, the RAHB interaction is less disturbed. In **2** the phenolic OH group acts as hydrogen donor, both for the RAHB and for the intermolecular interaction, but the last one with a larger interatomic O···O (2.38 Å) distance. In **3**, the intermolecular interaction affects the sp^3 hybridized oxygen atom of the phenolic group, turning its attached hydrogen into a more acidic atom. Indeed, the shortest O···O distance in the RAHB system is found for **3** (see Table 1).

3.3. Lattice and intermolecular energies

Lattice energy calculations (Table S2, ESI†) show that the dispersion energy (E_{disp}) is the major contribution towards the crystal stabilization for compounds **1**, **2** and **4** as generally expected for organic compounds, with similar percentages in the range 57.6 - 62.5 % and very similar total lattice energies. However, **3** shows a strong decrease in the dispersive component (34.9%) and an increase in the coulomb component (43.4%), probably due to the inclusion of the water molecule. Water contributes with strong tripartite hydrogen bond interactions, involving both the acceptor oxygen and the two donor hydrogen atoms. Molecular Docking analysis are in progress to measure the ability of the triazole derivatives as enzymatic activity inhibitors.

Moreover, because of this packing motif, the rotation of triazole ring is hindered around the simple C7-C8 bond, and the total lattice energy significantly decreases for compound **3** (-100.0 kJ mol^{-1}) when compared with the average of -125.6 kJ mol^{-1} for the remaining structures.

Intermolecular energy calculations from selected molecular pairs are shown in Table 2. The occurrence of strong N–H···O hydrogen bonds and offset π···π interactions is a common characteristic in all four structures. In **2** and **3**, the former is the most and higher interaction compared to pairs involving other types of contacts. Besides, π···π interactions are involved in molecular pairs with Pixel energies not only comparable with those of the N–H···O hydrogen bonds, but even having the highest pairing energy of -46.1 kJ/mol in structure **1**.

View Article Online
DOI: 10.1039/D0NJ02914A

Table 2. Selected Interaction energies (E_{TOT}), greater than 5 kJ/mol^{-1}, and their partitioned into coulombic, polarization, dispersion and repulsion contributions (kJ mol^{-1}) for various molecular pairs of **1** – **4**.

Comp.	Symmetry	Involved Interactions	*d*(H···A), ∠D—H···A	Centroid distance	E_{coul}	E_{pol}	E_{disp}	E_{rep}	E_{TOT}
1	1+x, y, z	N2-H2N···O2 N2-H2N···F1 N2-H2N···F2 O1-H10···N3 C6-H6···O1	2.11(3), 142 2.63(3), 139 2.60(2), 138 2.67(3), 123(2) 2.60(2), 126(2)	6.700	-35.4	-15.3	-27.4	33.5	-44.6
	1/2-x, 1/2+y, 1/2-z	C4-H4···N1 C5-H5···F3	2.90(2), 153(2) 2.74(2), 136(2)	10.851	-5.0	-1.4	-7.3	4.1	-9.6
	3/2-x,1/2+y,1/2-z	C3-H3···F3	2.68(2), 151(2)	10.930	-2.7	-0.7	-5.8	2.8	-6.4
	1-x,1-y,1-z	Cg1···Cg2	3.7001(2)[a]	4.566	-19.1	-5.1	-50.3	28.4	-46.1
	1-x,1-y, -z	Cg2···Cg2	3.8360(2)[a]	6.200	-11.4	-3.4	-37.6	21.3	-31.0
	-x, 1-y, -z	vdW[b]	---	8.145	-0.4	-1.3	-12.5	2.2	-12.0
	2-x,1-y,1-z	vdW[b]	---	7.224	-2.8	-1.1	-10.2	3.6	-10.6
2	-x,1-y,1-z	N3-H3···O1	2.24(3), 145	8.380	-57.3	-21.1	-18.6	30.0	-67.0
	3/2+x, 1/2-y, 1/2+z	C3-H3···N4, C3-H3···F3	2.70(3), 145 2.51(3), 155	9.769	-12.2	-3.3	-11.8	10.2	-17.1
	1/2-x, 1/2+y, 1/2-z	Cg1···Cg3	3.8267	7.049	-6.0	-1.7	-17.9	5.8	-19.8
	1-x,1-y,1-z	N3-H3N···O1	2.2447, 144.61	7.854	-13.3	-3.8	-21.4	9.9	-28.5
	3/2-x, -1/2+y, 3/2-z	O3-H3O···O2	2.377, 112	10.021	-5.0	-2.2	-10.2	8.8	-8.6
	-1+x, y, z	Cg1···Cg2	3.9407(2)[a]	5.019	2.4	-4.4	-40.0	18.6	-23.4
	1/2-x, -0.5+y, 3/2-z	vdW[b]	---	9.402	-2.3	-0.6	-7.2	3.1	-7.1
3	x, y, z	N2-H2A···O1W	1.845(2), 176	5.739	-71.9	-29.4	-10.1	63.3	-48.1
	1/2-x,3/2-y,1-z	C3-H3···F1	2.580(2), 147	6.407	-7.1	-2.8	-21.0	8.9	-22.0
	1/2+x, -1/2+y, z	O1W-H2W···O1	2.08(4), 166	6.201	-33.0	-13.6	-10.1	33.9	-22.7
	2-x, 1-y, 1-z	O1W-H1W···N3	2.14(3), 176	4.463	-33.3	-15.8	-13.1	36.9	-25.3
		O1W-H···O1W	---[(c)]	3.945	-5.6	-0.2	-0.8	0.1	-6.5
	1-x,1-y,1-z	C11-H11C···F3, Cg1···Cg1	2.430(2), 162 3.6317(2)[a]	5.667	-15.9	-6.9	-37.6	23.9	-36.5
	1-x, y, 1/2-z	F1-C10···N1[e]	3.7746, 160.5	6.564	-5.1	-1.6	-17.5	6.1	-18.2
	1-x, y, 3/2-z	C11-H11A···π	2.770, 158.80	9.050	-9.7	-4.6	-24.3	23.2	-15.3
	3/2-x, 3/2-y, 1-z	π···π	3.583	6.609	-4.1	-2.2	-30.8	12.8	-24.4
	-1/2+x, 3/2-y, -1/2+z	C4-H4···O2 C3-H3···F2 C11-H11B···O1	2.8138, 164.12 3.0502, 125.71 2.8464, 133.54	9.701	-4.9	-1.8	-11.4	5.6	-12.5
4	-1+x, y, z	N2-H2···O2, N2-H2···F2	2.06(3), 137 2.69(3), 130	6.640	-30.9	-14.4	-28.7	28.5	-45.6
	1-x,2-y,2-z	Cg1···Cg1	3.4895(5)[a]	6.176	-14.9	-4.2	-29.8	14.2	-34.7
	1-x,2-y,1-z	Cg2···Cg2	3.8922(5)[a]	7.689	-0.6	-1.0	-24.3	9.1	-16.8
	x,y,-1+z	C4-H4···N1	2.9617, 167.13	11.100	-5.1	-1.2	-8.8	4.0	-11.0
	1-x, 1-y, -z	F2-C10···N1[e]	3.668, 142.3	7.848	-6.8	-1.4	-15.4	7.7	-15.9
	1-x, 1-y, 1-z	π···π	3.601[d]	5.624	-4.3	-2.2	-37.7	16.3	-27.8
	2-x,1-y,1-z	C6-H6···Cl	3.2387, 159.62	8.129	-4.4	-2.0	-18.5	5.8	-19.1

[a] Inter-centroid distance: *C*g1 and *C*g2 are the centroids of N2-N4/C8-C9 and C1-C6 rings, respectively, for **1**; *C*g1, *C*g2 and Cg3 the centroids of N2-N4/C8-C9,C1-C6 and C1-C2-O3H-O-C4 rings, respectively, for **2**; *C*g1 is the centroid of N1-N3/C8-C9 ring for **3;** Cg1 and *C*g2 the centroids of N1-N3/C8-C9 and C1-C6 rings, respectively, for **4**. [b] vdW stands for van der Waals interaction. [c] Hydrogen atoms are not included because their positions are disordered. [d] Distance between Cg2 and the benzene ring plane of the neighbor molecule at 1-x, 1-y, 1-z. [e] Similar to halogen interactions, element from group IV to VI can form σ-hole interactions between an electrophiles group and a region rich in electrons or nucleophile. [59]

For the intermolecular hydrogen bonds O–H···O and O–H···N in **3**, where the water molecule participates, is observed that the interatomic distance H···Ow (2.08 Å) is shorter

View Article Online
DOI: 10.1039/D0NJ02914A

than the Hw···N (2.14 Å) in agreement with expected differences between homonuclear and heteronuclear hydrogen bonds. The energy results, showed in Table 2, also reveal that the largest contribution towards the crystal stabilization comes from the coulombic component (40.8 – 58.2 %) only for molecular pairs involving O–H···O and O–H···N hydrogen bonds. Moreover, the dispersion component clearly represents the dominant cohesive energy for π···π (67.5 – 90.1%) and remaining contacts.

3.4. Hirshfeld surface analysis

For a better comprehension of the crystal packing of **1** – **4**, a complete description of the main intermolecular interactions using Hirshfeld surface analysis was carried out. Figure 2 shows Hirshfeld surfaces (HSs) mapped over the d_{norm} property, where arrows with number indicate key contacts. Those with distances equal to the sum of van der Waals atomic radii (r_{vdW}) are represented as white regions and the contacts with distances shorter than and longer than van der Waals atomic radii (r_{vdW}) are shown as red and blue colors, respectively. Full 2D-fingerprint plots (FPs) of the main intermolecular contacts are depicted in Figure 3,

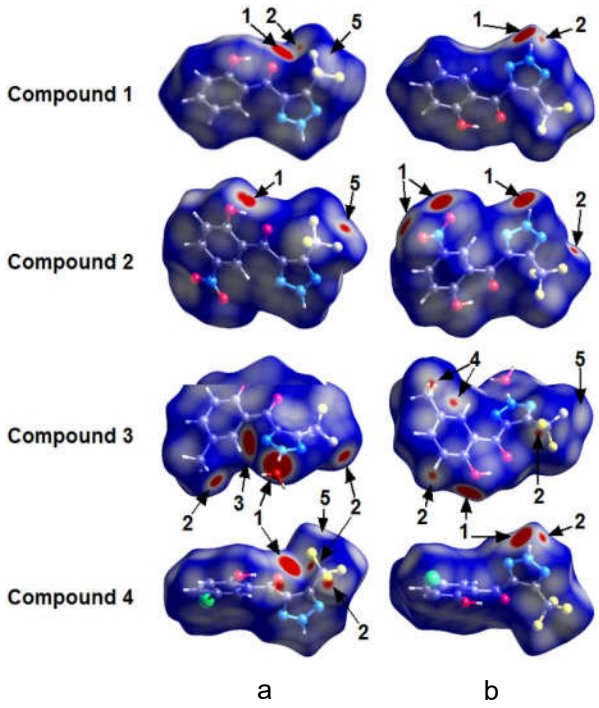

Figure 2. Hirshfeld surfaces of **1** – **4** mapped with d_{norm} in two orientations: (a) front view, (b) back view (180º rotated around the horizontal axis of the plot). Close contacts are labeled as follows: (1) O···H, (2) F···H, (3) N···H, (4) C···H, (5) F···F.

View Article Online
DOI: 10.1039/D0NJ02914A

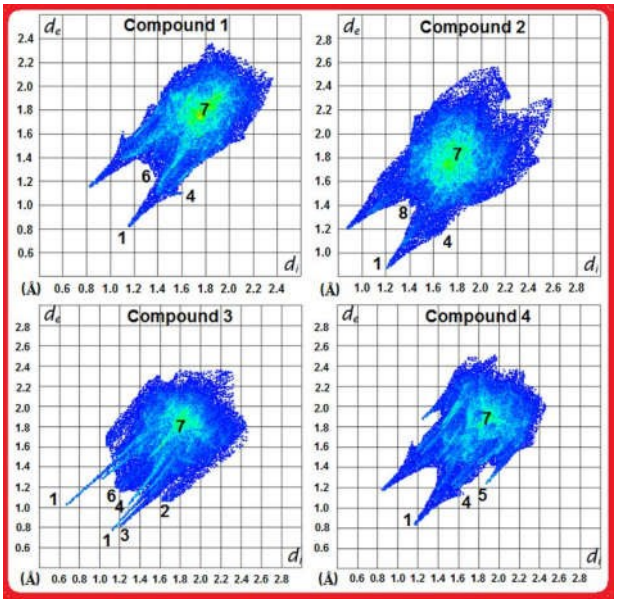

Figure 3. Full two-dimensional fingerprint plots for compounds **1** – **4**. Close contacts are labeled as follows: (1) O···H, (2) C···H, (3) N···H, (4) F···H, (5) Cl···H, (6) H···H, (7) C···C, (8) F···F.

The largest and red regions labeled 1 in Figure 2 dominate the d_{norm} maps for all the four structures. They are associated to the H···O/O···H contacts originated by strong N–H···O hydrogen bonds, except in compound **3** which also comes from the Ow-H···O hydrogen bond (Table 2). These contacts can be observed as a pair of symmetrical (except compound **3**) sharp spikes with a minimum distance (*de* + *di*) extending from 1.9 Å (in structure **3**) to 2.1 Å (in structure **2**) in the FPs (Figure). Similar contributions to overall HS area (see Figure S1, ESI†) are detected in the range 12 – 14 % for **1**, **3** and **4** and notably larger for **2** (23%), as result of the nitro group that not only doubles the number of oxygen atoms in the molecule but also these oxygen atoms contribute with hydrogen bonds because of their high acceptor character.

The presence of longer and sharper spikes in structure **3** indicates stronger and directional intermolecular interactions than those found for remaining structures, consistent with the geometric parameters listed in Table 2. In this structure the H···O/O···H interactions, labeled as 1, appear as two somewhat asymmetrical spikes. The longest spike labeled 1, at the top left region ($d_e > d_i$) of the FP, spread up to the shorter distance of (d_e + d_i) ≈ 1.7 Å and corresponds to points on the surface where the N2 triazole nitrogen atom acts as hydrogen donor and the water oxygen atom O1W as hydrogen acceptor establishing the N2-H2···O1W hydrogen bond. While the shortest spike labeled 1, at the bottom right region

View Article Online
DOI: 10.1039/D0NJ02914A

(d_e<d_i), span up to a distance of (d_e + d_i) ≈ 1.9 Å is associated with the O1W-H1W···O1 hydrogen bond between water protons and the phenolic O1 oxygen atom lone pairs.

The occurrence of small red spots (labeled 2) on the HSs showing H···F/F···H contacts is associated to weak N–H···F (**1** and **4**) or C–H···F (**2** and **3**) hydrogen bonds (see Table 2).[60,61] In the structures **1**, **3** and **4**, these contacts can also be observed as a pair of symmetrical sharp spikes labeled 4 at (*de* + *di*) ranging from 2.3 Å (compound **3**) to 2.8 Å (compound **4**) in the FPs, and account for high contributions of 21% and 22% to the overall HS area, respectively. The broad and bright-red spot labeled as 3 for compound **3** is due to H···N/N···H contacts associated to O1W–H1W···N3 hydrogen bonds, where the water molecule again causes the formation of the stronger H-bonds in the structure, as reflected by the highest electrostatic energies in comparison to that for C5–H5···F1 hydrogen bond (Table 2).

In addition to the above-mentioned hydrogen bonds, the crystal structure of compounds **1** – **4** features a significant contribution from π-stacking interactions (Table 2). They occur between layers of triazolyl rings (centroid *C*g1) for structures **3** and **4**, between layers of benzene rings (centroid *C*g2) for structures **1** and **4**, or between layers involving both type of rings as observed in **1** and **2** (see Table 2). C···C contacts appear as a distinct pale blue to green area labeled 7 at around *de* = *di* = 1.8 Å[62,63] in the FPs for all four compounds, with major contributions of 11 % and 5 % for structures **1** and **4**, respectively.

H···H contacts also operate in the crystal packing of all the four structures. These contacts are highlighted in the middle (labeled 6) of scattered points of FP maps with minimum values of (d_e + d_i) in the range 2.4 – 2.6 Å, and highest contributions of 13% and 20% to the total Hirshfeld surface for structures **1** and **3**, respectively, as result of the relative abundances of H-atoms in the respective molecules.

Although, HS shows F···F contacts as a small red area (labeled 5) for compound **2** (8.4% to HS), PIXEL calculations reveal a negligible energy contribution (-0.4 kJ / mol) for this interaction. A more detailed view of the fluorine region displays a high charge density in the interatomic zone, indicating probably a repulsive interaction.

It has been reported in literature[64] that in aromatic CHF molecules with high proportion of fluorine or low content of H-atoms, the C-F group prefers to form C–H···F hydrogen bonds rather than F···F contacts, due to the dipolar nature of the F···H interactions. These facts prompted to analyze the likelihood of occurrence of intermolecular F···H and F···F contacts, as well as other ones in the four compounds under study. The intermolecular interactions in

View Article Online
DOI: 10.1039/D0NJ02914A

1 – **4** were further assessed by using the enrichment ratio E_{XY},[65] and the values for selected contacts are listed in Table S3, ESI†, together with the discussion of the nature of some interactions (see ESI), while the relevance of the E_{XY} value in the most significant contacts are discussed briefly below.

The E_{OH} values in the range 1.45 – 2.07 in the studied compounds indicate the very high propensity to form homonuclear $H_O\cdots O$ hydrogen bonds, and particularly $H_{O/N}\cdots O$ polar hydrogen bonds (H atoms bound to O or N) involving in **3** a water molecule as revealed by observing the d_{norn} maps and FPs. Like in CHF data set, the E_{HF} values of 1.49 and 1.50 for **1** and **4**, respectively, indicate a high probability of occurrence of F···H contacts, in contrast with the related impoverished F···F contacts (E_{FH}= 0.80/0.59).

The C···C interactions in parallel π-stacking have a generally high probability to occur for all compounds, as reflected by the E_{CC} values near to unity in **2** (0.86), larger than unity in **3** (1.75), and even as high as 2.68 and 3.75 in compounds **4** and **1**, respectively, in accordance with the C···C contributions showed in Figure 3. In comparison, the enrichment of C···C contacts for our fluorinated CHFNO aromatic compounds tends to resemble that of CHF aromatic compounds previously reported,[65,66] which take a wide range of values between 0 and 4. Finally, it is interesting to notice the presence of rare short contacts (F···N for **1** and **4**; F···Cl for **4**; N···O for **2,** N···C for **2** and **4**, and C···Cl and O···Cl for **4**). They contribute in small proportion to total Hirshfeld surface in the range of C_{XY} = 3.4 – 7.1% (Table S4, ESI†), which are also notably enriched as reflected by the corresponding enrichment ratios larger than unity (see Table S3, ESI†).

A close exploration with *Shape index* and *Curvedness*, which are Hirshfeld surface properties generally used to identify planar π-stacking arrangements,[63] was performed. The pattern of touching red and blue triangles on the *shape index* surfaces (marked with arrows in Figure S2, ESI**†**, at left) is characteristic of π···π interactions,[62] and visible in all structures. This type of interaction is also evident as relatively large and green flat regions delineated by blue circles on the corresponding *Curvedness* surfaces(Figure S2, ESI†, at right).[62]

3.5. Vibrational analysis

The experimental IR and Raman spectra of **1** – **4** are shown in Figure S5, ESI† and **Table 3** summarizes the tentative assignment of some vibrational modes (Tables S10-S13, ESI† exhibit the complete vibrational assignment for **1** – **4**), principally associated with the pseudo ring -C-O-H···O=C-C. The prediction of the IR spectra were performed at B3LYP/6-31g (d,p) level, since the computed ones are close to the experimental, particularly when the O2-H···O1 is observed. The ν(O-H) is attributed to the strong band located at 3331 (Raman:

View Article Online
DOI: 10.1039/D0NJ02914A

3330 cm^{-1}), 3271, 3336 and 3334 cm^{-1} for **1** – **4**, respectively. In all compounds, O-H absorption shifts to lower frequencies than that expected for free species,[67,68] because of its participation in intramolecular hydrogen bonding interactions[67–70] (see Table 1).

Particularly, the lowest OH stretching frequency is observed for compound **2**, according to the increase of the OH distance. This can be attributed to the increase of the OH acidity by the influence of the *para* nitro group as shown in Scheme 2, causing a rise of the C7-O4 bond order and a lengthening of the O3-H distance. This is consistent with the DRX (see Table 1) and with the MEP results (see Figure S4, ESI†), where it can be observed that NO_2 group strongly attracts the electrons of the ring.

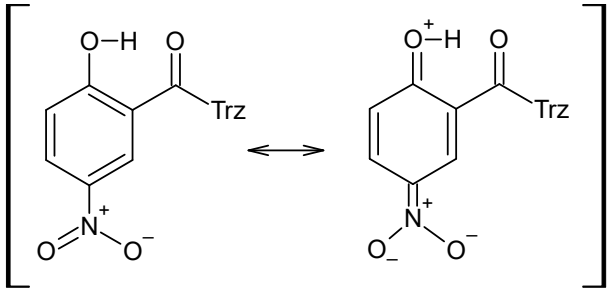

Scheme 2: Effect of the nitro group on the OH acidity by resonance.

The C=O stretching is attributed to the bands at 1603, 1617, 1612 y 1601 cm^{-1} (Raman: 1602, 1620, 1612 and 1603 cm^{-1}) for **1**, **2**, **3** and **4**, respectively, in accordance with observed C-O distances (see Table 1) and with reported values for conjugated ketones.[18,70]

The N-H stretching was assigned to the weak band at 3673 cm^{-1} for **2** (Table 3), while this mode was not observed in both IR and Raman for the other compounds.

From DRX results, it is observed that the N-H bond participates in intermolecular interactions (Figure 1) in all compounds. The δ(N-H) is assigned tentatively to the bands at 1426, 1428, 1427 y 1425 cm^{-1} for **1** – **4**, respectively.

In **2**, the NO_2 asymmetric and symmetric stretching bands are assigned to the IR absorptions at 1571 and to the intense band at 1342 cm^{-1} (Raman: 1573 and 1343 cm^{-1}), respectively. The high electronic density localized on the NO_2 group (Section 3.2),visualized in the molecular electrostatic potential map (Figure S4, ESI), is involved in strong intermolecular interactions (Figure 1b; Table 2). However, the frequencies of the NO_2 group are not substantially affected by hydrogen bonding interactions.[71,72] The NO_2 deformation is attributed to the strong IR band at 866 cm^{-1}. The experimental and calculated frequencies are in good agreement and with related molecules.[15,61]

The CH_3 symmetric stretching in **3** is located at 2928 cm^{-1} (Raman 2931 cm^{-1}), while the asymmetric and symmetric deformations at 1487 and 1382 cm^{-1}, respectively. In **4**, the IR

View Article Online
DOI: 10.1039/D0NJ02914A

and Raman bands at 1097 and 1093 cm^{-1}, respectively, are attributed to the C-Cl stretching.[17]

The heterocycle has characteristic bands, one of which is the ring deformation (δTRZ) assigned at 993, 995, 990 and 991 cm^{-1} for **1**, **2**, **3** and **4**, respectively. Besides, there is a vibration associated with the in-plane deformation of the benzene ring carbon atoms (δ (CCC)), located in the IR spectra at 919, 948, 950 and 938 cm^{-1} for **1**, **2**, **3** and **4**, respectively. This deformation together with ν_sCF_3 and δTRZ define a characteristic pattern for this family of compounds between 1100 and 900 cm^{-1}, as observed in Figure 4. Considering these results, it can be concluded that the ring substituents and intermolecular interactions have no major influence on ν_sCF_3 and δTRZ, but it is relevant in the deformation mode of the aromatic ring carbon atoms.

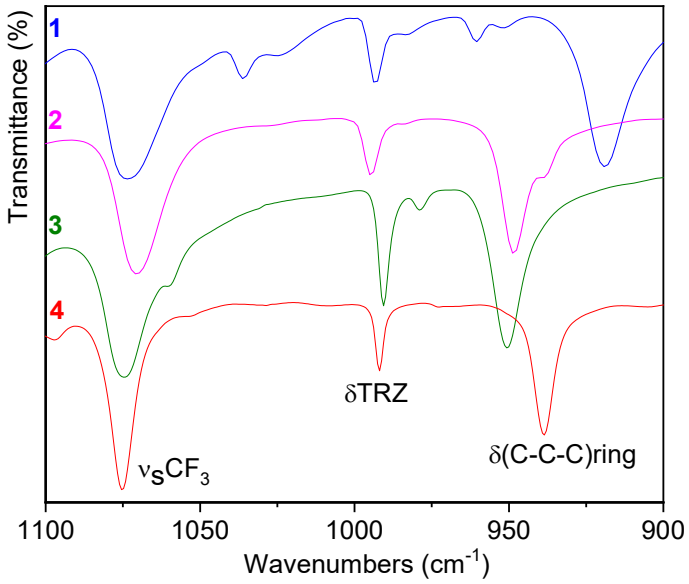

Figure 4. IR spectra of **1** – **4** in the range of 1100-900 cm^{-1}.

Table 3. Selected experimental and calculated frequencies and tentative fundamental vibration modes assignment of **1** – **4**.

Assignment[a]	1				2				3				4			
	Experimental[b]		Calculated[e]		Experimental[b]		Calculated[e]		Experimental[b]		Calculated[e]		Experimental[b]		Calculated[e]	
	IR[c]	Raman[d]	Freq.[b]	Int.[f]	IR[c]	Raman[d]	Freq.[b]	Int.[f]	IR[c]	Raman[d]	Freq.[b]	Int.[f]	IR[c]	Raman[d]	Freq.[b]	Int[f]
ν (N-H)			3660	143	3673(vw)		3654	152			3661	139			3658	147
ν (O-H)	3331(vs)	3330(23)	3295	316	3271(m)		3238	428	3336(vs)		3296	304	3334(vs)		3292	330
ν_s (CH_3)									2928(w)	2931(21)	3038	38				
ν (C=O)	1603(vs)	1602(69)	1661	60	1617(s)	1620(4)	1674	185	1612(m)	1612(3)	1662	80	1601(s)	1603(4)	1654	65
δ_{as} (CH_3)									1475(vs)	1476(34)	1514	36				
δ_s (CH_3)									1382(m)	1382(12)	1435	63				
ν_{as} (NO_2)					1571(s)	1573(13)	1636	102								
ν_s (NO_2)					1342(vs)	1343(100)	1392	431								
δ_s(NO_2)					866 (s)	865 (16)	878	53								
ν_{as} (CF_3)	1158(vs)		1218	252	1164(vs)		1218	242	1156(vs)		1218	252	1159(vs)		1219	256
ν (C-Cl)													1097(vw)	1093(11)	1120	39
ν_s (CF_3)	1073(vs)		1092	190	1070(vs)		1089	236	1074(vs)	1072(32)	1092	198	1075(vs)	1069(2)	1092	208
δ (TRZ)	993(m)	993(4)	1008	12	995(w)	994(4)	1009	11	990(m)	990(15)	1008	15	991(w)		1009	14
δ $(C=C)_{ar}$	919(vs)	919(<1)	934	118	948(s)	948(1)	970	100	950(vs)	949(11)	966	77	938(s)	932(1)	949	85

[a] ν, δ represent stretching and in plane deformation modes, respectively; [b] (cm^{-1}); [c] vs, very strong; s, strong; m, medium; w, weak; vw, very weak; [d] Intensity (arbitrary units); [e] B3LYP 6-31g(d,p); [f] Intensity (km/mol)

View Article Online
DOI: 10.1039/D0NJ02914A

3.6 Electronic spectra

The UV-Vis spectra were calculated with B3LYP/6-31g(d,p) and CAM-B3LYP/6-31g+(d,p), observing for the former a better fit with the experimental values. Table 4 shows the experimental and calculated (B3LYP/6-31g(d,p)) UV-Vis spectra in solid phase (using the diffuse reflectance accessory) of **1** – **4** (Figure S6, ESI†). Besides, Table S14 (ESI†) displays calculated wavelengths for **1** - **4**, using CAM-B3LYP functional and 6-31g+(d,p) basis set. The calculated molecular orbitals of each compound are presented in Figure S7-S10, ESI† and they were used to assist in the assignment of the observed absorptions. According to the results summarized in Table 4 the observed absorption bands of **1**, **3** and **4** are generated by electronic transitions between similar molecular orbitals. Thus, the bands at 212, 217 and 221 nm for **1**, **3** and **4**, respectively, are due to HOMO → LUMO+3 excitations, from π orbitals of the aromatic ring and non bonding orbitals of both oxygen (and chlorine for **4**) atoms**,** to π* of both rings and the C-O(H) bond. The absorption at 221 nm has also the contribution of HOMO-1 → LUMO+1 transition, involving the *p* orbitals of fluorine atoms as well.

The observed band at 250 nm for **2** is generated by dominant HOMO-2 → LUMO transitions which corresponds to π→π* excitation from the aromatic fragment and non-bonding orbitals of the carbonyl and nitro oxygen atoms to both rings.

The absorptions at 269, 271 and 268 nm for **1**, **3** and **4**, respectively, are mainly attributed to a sole one electron excitations from HOMO-1 to LUMO orbitals. They can be assigned to transitions from π orbitals of the aromatic fragment to π* of both rings, excluding the N1 atom. The dominant HOMO→ LUMO excitation is attributed to the observed bands at 361, 322, 369 and 372 nm for **1**, **2**, **3** and **4**, respectively. They are substantially dominated by transitions from π of the benzene and non-bonding orbitals of both oxygen atoms (including both nitro oxygen atoms for **2** and chlorine atom for **4**) to π* orbitals of the whole molecule except for N1 atom. Figure 5 shows the energy level diagram (in eV) for the calculated frontier molecular orbitals of **1** – **4**. The HOMO and LUMO orbitals stabilization in **2** could be attributed to the presence of the NO_2 group on the benzene ring. Table S15 (ESI†) displays the HOMO–LUMO energy gaps ($\Delta E_{H\text{-}L}$) for **1** – **4** calculated with CAM-B3LYP approximation, which resulted much higher than those obtained with B3LYP functional.

View Article Online
DOI: 10.1039/D0NJ02914A

Table 4. Experimental and calculated electronic spectra (in nm) for **1** – **4**, and tentative assignment of the absorption bands.

Comp.	Exp.[a, b]	Calc.[a,c]	*f*[d]	Assignment	%
1	212	203	0,0991	HOMO → LUMO+3	44
	269	274	0,2066	HOMO-1 → LUMO	93
	361	364	0,077	HOMO→LUMO	100
2	250	266	0,3421	HOMO-2 →LUMO	86
	322	345	0,0818	HOMO→LUMO	100
3	217	200	0,0986	HOMO→LUMO+3	31
				HOMO-6→LUMO	33
	271	273	0,2127	HOMO-1→LUMO	72
	369	377	0,0775	HOMO→LUMO	100
4	221	206	0,2510	HOMO→LUMO+3	41
				HOMO-1→LUMO+1	31
	268	270	0,1751	HOMO-1→LUMO	59
				HOMO→LUMO+1	39
	372	383	0,0803	HOMO→LUMO	100

[a]In nm. [b]Diffuse Reflectance. [c] B3LYP/6-31G(d,p). [d]Oscillator strength in atomic units.

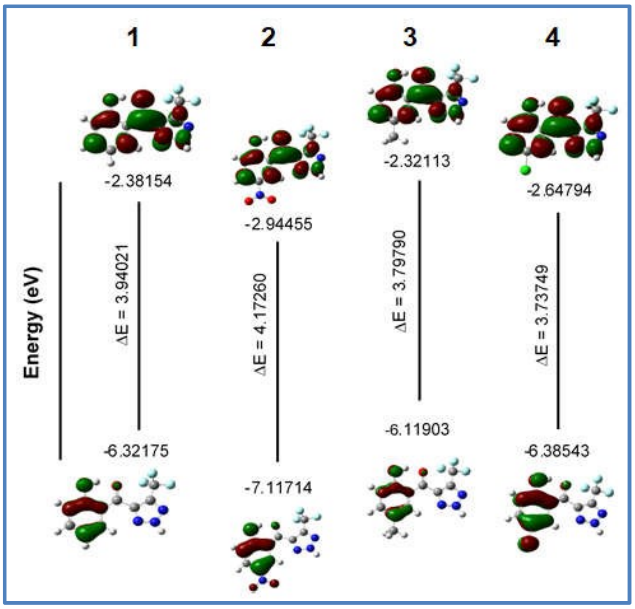

Figure 5: Calculated frontier MO energies (eV), and ΔHOMO-LUMO gaps for **1** – **4**.

View Article Online
DOI: 10.1039/D0NJ02914A

3.7. Quantum chemical calculations and NBO analysis

The geometry of **1** – **4**, obtained from single X-ray diffractions data, were optimized for free molecules at B3LYP/(6-31g(d,p); 6-311++g(d,p)) and cc-pVDZ level of theory, and their computed geometrical parameters were compared with those in solid state (see Tables S5-S9, ESI†).

Although the Pople basis set (6-31g(d,p) and 6-311++g(d,p)) (with B3LYP) reproduce fairly well the experimental geometries, the NBO calculations were performed with the Dunning base B3LYP-cc-PVDZ which was the most suitable for the all the structures allowing to compare the obtained results (see Tables S4-S8, ESI†).

Figure S3, ESI† shows the optimized geometries of **1** – **4** (B3LYP 6-31g(d.p), and the MEP (molecular electrostatic potential) maps (see Figure S4, ESI†) show, around the N-H acidic hydrogen atom of the heterocycle, the most electrophilic zone in all compounds. Whereas, the nucleophilic sites are located on the oxygen atoms of the -NO_2 group for **2** and OH and CO groups for **1**, **3** and **4**.

Natural Bond Orbital (NBO) analysis is a useful technique that allow to study intra- and intermolecular interactions among organic systems, considering bond interactions and conjugative effects. The interaction energy between donor and acceptor NBO orbitals is evaluated using the matrix Fox second-order perturbation theory (E(2))[54] and its magnitude depends on the electron donating tendency from donors to acceptors and the extent of conjugation throughout the system. Hence, the charge transfer between the lone pairs (n or π) of nucleophilic (Y-A) donor groups and the anti-bonding orbital (σ^*) of electrophilic (D-X) acceptor groups is a measure of the D-X···A-Y strength interaction and enables a qualitative description of that interactions. In the studied systems the interaction energies $E^{(2)}$ between intra- and intermolecular NBO orbitals were calculated, at B3LYP/6-31G(d,p) theory level and are listed in Table 5.

The NBO intramolecular interactions energies were evaluated for monomers with optimized (at the same level of theory) and experimental geometries, obtained from X-ray crystallographic data. For **2**, the NBO analysis (calculated and experimental) indicates that both intra-molecular hydrogen bonding energy are close to each other and stronger than for the rest of the compounds. Furthermore, for **1**, **3** and **4**, E(2) resulted quite different for calculated and experimental geometries (see Table 5). These results might be rationalized considering the acidic nature of the phenolic H atom in **2**, favored by the NO_2 substituent, causing a hyper-conjugative interaction. This interaction involves a higher partial transfer (CT) from one lone pair of the O2 atom to the σ^* O1-H acceptor orbital, LP O2 → σ^*(O1-H).

View Article Online
DOI: 10.1039/D0NJ02914A

A second less energetic intramolecular interaction is also predicted in all geometry optimized monomers, in which the electron lone pair of the N3 atom transfers charge to the empty σ*(C6–H6) orbital [LPσN3→σ*C(6–H6)]. This partial CT is also observed for the molecular geometry in the crystalline state of **1** and **2** but not for **3** and **4**, probably because in the last systems the molecular conformation in the crystal deviate significantly from the planarity observed in free molecule (see figure S11, ESI†).

NBO analysis of selected intermolecular interactions, described in Table 2, were performed on dimers constructed from X-ray diffraction data to complement the results of the interaction energies calculated with Pixel program.

The mentioned intermolecular interactions were modeled by building three dimers (for **1**), four dimers (for **2**), three dimers and a tetramer (for **3**), and five dimers (for **4**). Dimers of **1** and **4** are shown in Figure S12, ESI† (for **2** and **3**, see Figures S13-S14, ESI†). In both **1** and **4,** the only intermolecular interaction that exhibits significant CT is the N2-H2N···O2 hydrogen bonding, which consist in a partial electron transfer from one of the carbonyl oxygen lone pairs (LPO2) from one molecule, towards the σ*(N-H2H) orbital of the other molecule, see Table 5. For **1** the second order perturbation energy $E^{(2)}$ value is less than for **4**, because the O2···H2N2 distance in the latter (see Table 2) is shorter favoring the overlapping of electron donor and acceptor orbitals. In compound **2**, significant values of the second-order perturbation energy $E^{(2)}$ were observed for N3-H3···O1 (6.3 kJ/mol) and O3-H3O···O2 (8.5 kJ/mol) intermolecular hydrogen bonds. The lone pairs of both O1 and O2 oxygen atoms belonging to the nitro group act as electron donors. The last energy value corresponds to a partial CT from O2 lone pairs to the σ*(O3-H3O) acceptor orbital [LPO2(3)→σ*O3–H3O(1)]and the former energy value is due to the O1 lone pairs overlapped with the σ*(N3–H3) orbital [LPO1(2)→σ*N3–H3(1)]. Moreover, in compound **3**, the largest values of the second-order perturbative energy $E^{(2)}$, involve the interaction of the water and triazole orbitals. In decreasing order of $E^{(2)}$ energy values they are: a) the interaction of one lone pair (LP) of water O1W with the σ*(N2–H2A) antibonding orbital of the triazole group [LPO1W→σ*(N2–H2A)], 47.9 kJ/mol; b) the interactions of the LP of N3 triazole nitrogen atom with the σ*(O1-H1W) antibonding orbital of the water molecule, 17.0 kJ/mol, and c) the LP of O1 hydroxyl oxygen atom with other σ*(O1W-H2W) antibonding orbital of other water molecule,10.5 kJ/mol.

View Article Online
DOI: 10.1039/D0NJ02914A

For the remaining dimers, charge transfers of type F···H, O···H, N···H and/or Cg···Cg were also observed, with energies much lower than 4.184 kJ / mol. The atomic charges (NPA) for the experimental monomers and dimers are described in ESI† section (Table S16: **1** and **4**, Table S17: **2**, and Table S18: **3**).

Table 5. NBO intra e intermolecular interactions energies (kJ/mol) calculated at B3LYP/cc-PVDZ theory level.

	Donor NBO (i)	Acceptor NBO (j)	$E^{(2)}$ [kJ/mol] **1**	**2**	**3**	**4**
Monomers *(Optimized)*	LP n O2	→ σ* O1– H	59.2 *(132.6)*	123.8 *(140.5)*	62.8 *(132.0)*	31.3 *(134.1)*
	LP σ N30	→ σ* C6– H60	5.0 *(9.9)*	2.3 *(14.3)*	*(10.1)*	*(13.98)*
Selected Dímers	LP n O2 (2)	→ σ* N2– H2N (1)	9.0		0,0	0,0
	LP π F1(2)	→ σ* N2– H2N (1)	0.7	0,0	0,0	0,0
	LP π F2(2)	→ σ* N2– H2N (1)	0.8	0,0	0,0	0,0
	LP n O1(2)	→ σ* C6– H6(1)	1.3		0,0	0,0
	LP σ N3(1)	→ σ* O1– H1(2)	3.3	0,0	0,0	0,0
	LP O1(1)	→ σ* N3– H3(2)	0,0	6.3	0,0	0,0
	LP σ O2(3/1)	→ σ* O3– H3O(1/3')		8.5		
	LP σ N4(4/1)	→ σ* C5– H5(1/4')	0,0	3.4	0,0	0,0
	LP F3(4/1)	→ σ* C5– H5(1/4')	0,0	3.1	0,0	0,0
	LP π F3(1)	→ σ* C10– F3(5)	0,0	0.4	0,0	0,0
	LP O1W(2)	→ σ* N2– H2A(1)	0,0	0,0	47.9	0,0
	LP σ N3(1)	→ σ* O1W– H1W(2)	0,0	0,0	17.0	
	LP O1(1)	→ σ* O1W– H2W (2)	0,0	0,0	10.5	0,0
	LP σ N1(1)	→ σ* C6– H6(3)	0,0	0,0	1,4	
	LP F3(1)	→ σ* C11– H11(3)	0,0	0,0	2.8	0,0
	LP σ F1(1)	→ σ* C5– H5(4)	0,0	0,0	0.8	0,0
	LP π F3(1)	→ σ* C10– F3(5)	0,0		0.2	
	LP O2(2)	→ σ* N2– H2N(1)	0,0	0,0	0,0	16.5
	LP F1(2)	→ σ* N2– H H2N (1)	0,0	0,0	0,0	3.4
	LP π F2(2)	→ σ* N2– H H2N (1)	0,0	0,0	0,0	0.7
	LP σ N3(1)	→ σ* O1– H1(2)0	0,0	0,0	0,0	1.1

View Article Online
DOI: 10.1039/D0NJ02914A

Conclusions

The molecules are composed of two planar rings connected to a central carbonyl group. The arrangement of the triazole ring respect to the C=O plane is strongly influenced by intermolecular interactions within the crystal lattice. However, the *o*-hydroxyphenyl and carbonyl moieties are almost co-planar because of the intramolecular hydrogen bond that connects them and limits the free rotation between the planes. This structural portion is further involved in an enol-keto / keto-enol tautomerism. A detailed inspection of the bond distances within the pseudo-ring shows a strong prevalence of the enol-keto form favored by the aromatic resonance stabilization. The differences between compounds were attributed to the intermolecular interactions. The triazole ring has expected interatomic distances for this kind of heterocycle. The C-C single bond (1.397 Å – 1.408 Å) in the ring is noticeably shorter than the exocyclic C7-C8 (1.484 Å – 1.490 Å) with the same sp^2 hybridization pattern, showing a strong delocalization charge.

The structural motifs of **1** – **4** are dominated by intermolecular interactions between the acidic hydrogen (N-H/O-H) and the acceptor lone pairs of N and O atoms. The stacking in the crystal packing is complemented with extensive $\pi\cdots\pi$ contacts involving mainly aromatic rings. The nature and strength of the interactions were evaluated and quantified using the Pixel program and Hirshfeld surface analysis, which enable the localization of the most relevant contacts. The differences that a water molecule (crystal of **3**) causes in the intermolecular interactions shows the high predisposition of the studied compounds to interact with polar sites, such as that in a protein.

The results of NBO calculations evidenced the existence of an additional stabilization, arising from the intermolecular charge transfer of the oxygen lone pairs to the acceptor antibonding orbitals of N-H and O-H hydrogen bonds.

The intra and intermolecular interactions were evidenced in the vibrational spectra by the band shiffting of the groups directly involved in them. The location and shape of the νOH, ν(C=O) and ν(C-O) absorption bands reveal their participation in strong intramolecular interactions and, particularly in **2**, also in intermolecular contacts. The vibration associated with the in plane deformation of the benzene ring carbon atoms, δ (CCC) is sensitive to the ring substituents and intermolecular interactions.

The dominant predicted HOMO $\rightarrow$ LUMO transitions for **1** – **4** involve essentially excitations from the aromatic ring to orbitals of the whole molecule. The absorption values are similar for compounds **1**, **3** and **4**, revealing that this transition is not affected by the substitution of the benzene ring. However, the shifting of the HOMO-LUMO excitation to lower wavelength in **2** could be attributed to the nitro group. According to DFT calculations, the computed

View Article Online
DOI: 10.1039/D0NJ02914A

energies of HOMO and LUMO orbitals for compound 2 present the lowest values with respect to **1**, **3** and **4**, indicating that both could be stabilized by the NO_2 group, giving rise to the largest energy gap (ΔHOMO-LUMO).

Supporting Information Available

Table S1. Crystal data and structure refinement results for compounds **1-4**; **Table S1**. Lattice energies (kJ mol^{-1}) partitioned into coulombic (Ecoul), polarization (Epol), dispersion (Edisp) and repulsion (Erep) components for **1** – **4**. **Table S3.** Enrichment ratio (EXY)*of selected intermolecular contacts for compounds **1** – **4**; **Table S4.** Hirshfeld contact surfaces CXY(%)*, proportion of chemical type on the molecular surface Sx (%), and random contacts RXY(%) of intermolecular interactions for compounds **1** – **4**; **Table S5.** Calculated geometrical parameters of pseudo ring of **1** – **4**; **Table S6.** Experimental and calculated geometrical parameters of **1**: **Table S7.** Experimental and calculated geometrical parameters of **2**; **Table S8.** Experimental and Calculated geometrical parameters of **3**; **Table S9.** Experimental and Calculated geometrical parameters of **4**; **Table S2 – S13**. Experimental and calculated frequencies and tentative assignment of fundamental vibration modes of **1** – **4**. **Table S14.** Experimental and calculated electronic spectra (CAM-B3LYO/6-31g+(d,p)) for **1** – **4**; **Table S15.** Calculated frontier MO energies and ΔHOMO-LUMO gaps (eV) for **1** – **4**. **Table S16.** Natural Population Analysis for **1** and **4**; **Table S17.** Natural Population Analysis for **2**; **Table S18.** Natural Population Analysis of **3**. **FigureS1.** Relative contributions of selected intermolecular contacts to the Hirshfeld surface area for structures **1** – **4**. **Figure S2.** Hirshfeld surfaces for **1-4**, mapped over: (a) shape index, highlighting the regions involved in π-stacking interactions, and (b) curvedness; **Figure S3.** Optimized geometries calculated with B3LYP 6-31g(d.p): a. **1**. b. **2**. c. **3** and d. **4**; **Figure S4.** Molecular electrostatic potential maps (MEPs) calculated with B3LYP 6-31g(d.p): a. **1**. b. **2**. c. **3** and d. **4**; **Figure S5.** Infrared (upper trace, KBr pellets) and Raman (lower trace) spectra of the solid at room temperature of: a. **1**. b. **2**. c. **3** and d. **4**; **Figure S6.** Calculated and experimental electronic spectra of **1** – **4**; **Figure S7.** Molecular orbitals involved in the electronic transitions of **1**. The energy scale is only qualitative and does not represent the actual energy of the molecular orbitals; **Figure S8.** Molecular orbitals involved in the electronic transitions of **2**. The energy scale is only qualitative and does not represent the actual energy of the molecular orbitals; **Figure S9.** Molecular orbitals involved in the electronic transitions of **3**. The energy scale is only qualitative and does not represent the actual energy of the molecular orbitals; **Figure S10.** Molecular orbitals involved in the electronic transitions of **4**. The energy scale is only

View Article Online
DOI: 10.1039/D0NJ02914A

qualitative and does not represent the actual energy of the molecular orbitals; **Figure S11.** Calculated (B3LYP/cc-PVDZ, red) and experimental geometries (green) for: a. **3** and b. **4**; **Figure S12.** Dimers of: a. **1** and b. **4**; **Figure S13.** Dimers of **2**. a. I and b. II; **Figure S14.** Dimer of **3**.

Acknowledgements

The authors thank CONICET (Grant PIP 11220130100651CO and PIP 0359), UNLP (Grants 11/X709, 11/X673, 11/X830 and 11/X848) and Departamento de Ciencias Básicas - Universidad Nacional de Luján (UNLu) for financial support. G.A.E., O.E.P and S.E.U are research fellows and E.E.C. is a scholarship holder of CONICET. J.L.J is a research fellow of Comisión de Investigaciones Científicas de la Prov. de Buenos Aires (CIC). S.E.U and J.L.J especially thank Deutscher Akademischer Austauschdienst Germany (DAAD) for financial support.

View Article Online
DOI: 10.1039/D0NJ02914A

References

1 A. C. Tomé, *Sci. Synth.*, 2004, 415–601.

2 D. D. Díaz, M. G. Finn, K. B. Sharpless, V. Fokin and J. Hawker, *An. Química*, 2008, **104**, 173–180.

3 J. Totobenazara and A. J. Burke, *Tetrahedron Lett.*, 2015, **56**, 2853–2859.

4 D. Dheer, V. Singh and R. Shankar, *Bioorg. Chem.*, 2017, **71**, 30–54.

5 N. Kerru, L. Gummidi, S. Maddila, K. K. Gangu and S. B. Jonnalagadda, *Molecules*, 2020, **25**, 1–42.

6 J.-J. Yang, W.-W. Yu, L.-L. Hu, W.-J. Liu, X.-H. Lin, W. Wang, Q. Zhang, P.-L. Wang, S.-W. Tang, X. Wang, M. Liu, W. Lu and H.-K. Zhang, *J. Med. Chem.*, 2020, **63**, 569—590.

7 E. Bonandi, M. S. Christodoulou, G. Fumagalli, D. Perdicchia, G. Rastelli and D. Passarella, *Drug Discov. Today*, 2017, **22**, 1572–1581.

8 W. K. Hagmann, *J. Med. Chem.*, 2008, **51**, 4359–4369.

9 K. Muller, C. Faeh and F. Diederich, *Science (80-.)*., 2007, **317**, 1881–1886.

10 C. Upadhyay, M. Chaudhary, R. N. De Oliveira, A. Borbas, P. Kempaiah, P. S and B. Rathi, *Expert Opin. Drug Discov.*, 2020, **15**, 705–718.

11 B. M. Johnson, Y.-Z. Shu, X. Zhuo and N. A. Meanwell, *J. Med. Chem.*, 2020, **63**, 6315–6386.

12 S. A. Usachev, B. I. Usachev, O. S. Eltsov and V. Y. Sosnovskikh, *Tetrahedron*, 2014, **70**, 8863–8871.

13 V. Y. Sosnovskikh and B. I. Usachev, *Mendeleev Commun.*, 2002, **12**, 75–76.

14 I. C. H. Castañeda, S. E. Ulic, C. O. D. Védova, N. Metzler-Nolte and J. L. Jios, *Tetrahedron Lett.*, 2011, **52**, 1436–1440.

15 L. P. Avendaño Jiménez, G. A. Echeverría, O. E. Piro, S. E. Ulic and J. L. Jios, *J. Phys. Chem. A*, 2013, **117**, 2169–2180.

16 N. Belskaya, J. Subbotina and S. Lesogorova, in *Topics in Heterocyclic Chemistry*, 2014, vol. 10, pp. 51–116.

17 E. Pretsch, P. Bühlmann and M. Badertscher, *Structure determination of organic compounds: Tables of spectral data*, 2009.

18 D. Lin-Vien, N. B. Colthup, W. G. Fateley and J. G. Grasselli, *The Handbook of Infrared and Raman Characteristic Frequencies of Organic Molecules*, San Diego, EEUU, 2nd Decemb., 1991.

19 V. Bertolasi and G. Gilli, *In The Chemistry of Enols. Chapter 13.*, Nueva York, 1990.

View Article Online
DOI: 10.1039/D0NJ02914A

20 G. Gilli, F. Bellucci, V. Ferretti and V. Bertolasi, *J. Am. Chem. Soc.*, 1989, **111**, 1023–1028.

21 V. Bertolasi, P. Gilli, V. Ferretti and G. Gilli, *J. Am. Chem. Soc.*, 1991, **113**, 4917–4925.

22 P. Gilli, V. Bertolasi, V. Ferretti and G. Gilli, *J. Am. Chem. Soc.*, 1994, **116**, 909–915.

23 V. Bertolasi, P. Gilli, V. Ferretti and G. Gilli, *J. Chem. Soc. Perkin Trans. 2 Phys. Org. Chem.*, 1997, 945–952.

24 P. Gilli, V. Bertolasi, L. Pretto, V. Ferretti and G. Gilli, *J. Am. Chem. Soc.*, 2004, **126**, 3845–3855.

25 V. Bertolasi, L. Pretto, G. Gilli and P. Gilli, *Acta Crystallogr. Sect. B Struct. Sci.*, 2006, **62**, 850–863.

26 X. Lin, H. Zhang, X. Jiang, W. Wu and Y. Mo, *J. Phys. Chem. A*, 2017, **121**, 8535–8541.

27 X. Jiang, H. Zhang, W. Wu and Y. Mo, *Chem. - A Eur. J.*, 2017, **23**, 16885–16891.

28 J. M. Guevara-Vela, E. Romero-Montalvo, A. Costales, Á. M. Pendás and T. Rocha-Rinza, *Phys. Chem. Chem. Phys.*, 2016, **18**, 26383–26390.

29 T. M. Krygowski and J. E. Zachara-Horeglad, *Tetrahedron*, 2009, **65**, 2010–2014.

30 A. V. Gurbanov, M. L. Kuznetsov, S. D. Demukhamedova, I. N. Alieva, N. M. Godjaev, F. I. Zubkov, K. T. Mahmudov and A. J. L. Pombeiro, *CrystEngComm*, 2020, **22**, 628–633.

31 S. J. Grabowski, *Hydrogen Bonding—New Insights*, Springer Netherlands, 2006.

32 A. Gavezzotti, *New J. Chem.*, 2011, **35**, 1360–1368.

33 S. K. Seth, D. Sarkar, A. D. Jana and T. Kar, *Cryst. Growth Des.*, 2011, **11**, 4837–4849.

34 A. Saeed, M. Bolte, M. F. Erben and H. Pérez, *CrystEngComm*, 2015, **17**, 7551–7563.

35 V. Y. Sosnovskikh and B. I. Usachev, 2000, **49**, 2074–2076.

36 CrysAlisPro, Oxford Diffraction Ltd., version 1.171.33.48 (release 15-09-2009 CrysAlis171.NET).

37 G. M. Sheldrick, *Acta Crystallogr. Sect. A Found. Crystallogr.*, 2008, **64**, 112–122.

38 L. J. Farrugia, *J. Appl. Crystallogr.*, 2012, **45**, 849–854.

39 A. L. Spek, *Acta Crystallogr. Sect. D Biol. Crystallogr.*, 2009, **65**, 148–155.

40 A. L. Spek, PLATON – A Multipurpose Crystallographic Tool, Utrech University, Utrech, The Netherlands, (2011).

41 L. J. Farrugia, *J. Appl. Crystallogr.*, 1997, **30**, 565–565.

42 C. F. Macrae, I. J. Bruno, J. A. Chisholm, P. R. Edgington, P. McCabe, E. Pidcock, L.

View Article Online
DOI: 10.1039/D0NJ02914A

Rodriguez-Monge, R. Taylor, J. Van De Streek and P. A. Wood, *J. Appl. Crystallogr.*, 2008, **41**, 466–470.

43 A. Gavezzotti, *J. Phys. Chem. B*, 2002, **106**, 4145–4154.

44 A. Gavezzotti, *J. Phys. Chem. B*, 2003, **107**, 2344–2353.

45 G. E. M. J. Frisch, G. W. Trucks, H. B. Schlegel, K. N. Scuseria, M. A. Robb, J. R. Cheeseman, J. A. Montgomery, Jr., T. Vreven, B. M. Kudin, J. C. Burant, J. M. Millam, S. S.Iyengar, J. Tomasi, V. Barone, K. M. Cossi, G. Scalmani, N. Rega, G. A. Petersson, H. Nakatsuji, M. Hada, M. Ehara, H. Toyota, R. Fukuda, J. Hasegawa, M. Ishida, T. Nakajima, Y. Honda, O. Kitao, C. A. Nakai, M. Klene, X. Li, J. E. Knox, H. P.Hratchian, J. B. Cross, V. Bakken, C. J. Jaramillo, R. Gomperts, R. E. Stratmann, O. Yazyev, A. J. Austin, R. Cammi, J. J. Pomelli, J. W. Ochterski, P. Y. Ayala, K. Morokuma, G. A. Voth, P. Salvador, O. F. Dannenberg, V. G. Zakrzewski, S. Dapprich, A. D. Daniels, M. C. Strain, A. G. D. K. Malick, A. D.Rabuck, K. Raghavachari, J. B. Foresman, J. V. Ortiz, Q. Cui, I. Baboul, S. Clifford, J. Cioslowski, B. B. Stefanov, G. Liu, A. Liashenko, P. Piskorz, A. Komaromi, R. L. Martin, D. J. Fox, T. Keith, M. A. Al-Laham, C. Y. Peng, C. Nanayakkara, M. Challacombe, P. M. W. Gill, B. Johnson, W. Chen, M. W. Wong and J. A. P. Gonzalez, 2004.

46 J. J. McKinnon, M. A. Spackman and A. S. Mitchell, *Novel tools for visualizing and exploring intermolecular interactions in molecular crystals*, 2004, vol. 60.

47 J. J. McKinnon, D. Jayatilaka and M. A. Spackman, *Chem. Commun.*, 2007, 3814.

48 M. A. Spackman, *Phys. Scr.*, 2013, **87**, 048103.

49 M. A. S. S. K. Wolff, D. J. Grimwood, J. J. McKinnon, M. J. Turner, D. Jayatilaka, *CrystalExplorer (Version 3.0). Univ. West. Aust.*

50 A. D. Becke, *J. Chem. Phys.*, 2014, **140**, 18A301.

51 A. D. McLean and G. S. Chandler, *J. Chem. Phys.*, 1980, **72**, 5639–5648.

52 M. T. Nguyen, E. S. Kryachko and L. G. Vanquickenborne, *General and Theoretical Aspects of Phenols*, 2003.

53 H. Lampert, W. Mikenda and A. Karpfen, *J. Phys. Chem.*, 1996, **3654**, 7418–7425.

54 A. E. Reed, L. A. Curtiss and F. Weinhold, *Chem. Rev.*, 1988, **88**, 899–926.

55 B. I. Usachev, S. A. Usachev, G. V. Röschenthaler and V. Y. Sosnovskikh, *Tetrahedron Lett.*, 2011, **52**, 6723–6725.

56 P. Gilli, V. Bertolasi, L. Pretto, L. Antonov and G. Gilli, *J. Am. Chem. Soc.*, 2005, **127**, 4943–4953.

57 L. Pauling, *J. Am. Chem. Soc.*, 1947, **69**, 542–553.

58 C. Janiak, *J. Chem. Soc. Dalt. Trans.*, 2000, 3885–3896.

View Article Online
DOI: 10.1039/D0NJ02914A

59 J. S. Murray, P. Lane and P. Politzer, *J. Mol. Model.*, 2009, **15**, 723–729.

60 P. Panini and D. Chopra, *Cryst. Growth Des.*, 2014, **14**, 3155–3168.

61 C. D. Alcívar León, G. A. Echeverría, O. E. Piro, S. E. Ulic, J. L. Jios, J. A. Pereañez, I. C. Henao Castañeda and H. Pérez, *New J. Chem.*, 2017, **41**, 14659–14674.

62 M. A. Spackman and D. Jayatilaka, *CrystEngComm*, 2009, **11**, 19–32.

63 A. Di Santo, G. A. Echeverría, O. E. Piro, H. Pérez, A. Ben Altabef and D. M. Gil, *J. Mol. Struct.*, 2017, **1134**, 492–503.

64 V. R. Thalladi, H.-C. Weiss, D. Bläser, R. Boese, A. Nangia and G. R. Desiraju, *J. Am. Chem. Soc.*, 1998, **120**, 8702–8710.

65 C. Jelsch, K. Ejsmont and L. Huder, *IUCrJ*, 2014, **1**, 119–128.

66 C. Jelsch, S. Soudani and C. Ben Nasr, *IUCrJ*, 2015, **2**, 327–340.

67 K. Nakamoto, *Infrared and Raman Spectra of Inorganic and Coordination Compounds: Part A: Theory and Applications in Inorganic Chemistry*, 2009.

68 P. J. Larkin, *'IR and Raman Spectroscopy - Principles and Spectral Interpretation'*, 2011.

69 Z. Rappoport, *The Chemistry of enols.*, John Wiley & Sons Australia, Limited, 1990.

70 L. J. Bellamy, *The Infrared Spectra of Complex Molecules*, 1980, vol. 2.

71 N. Sundaraganesan, S. Ilakiamani, H. Saleem, P. M. Wojciechowski and D. Michalska, *Spectrochim. Acta Part A Mol. Biomol. Spectrosc.*, 2005, **61**, 2995–3001.

72 D. Mahadevan, S. Periandy and S. Ramalingam, *Spectrochim. Acta Part A Mol. Biomol. Spectrosc.*, 2011, **84**, 86–98.

DOI: 10.1039/D0NJ02914A

Table of Contents

Comprehensive theoretical, structural and spectroscopic investigations on new substituted 1,2,3-triazoles in solid state.